Cost-Function Extremum Seeking Based Model Predictive Torque Control of PMSM With Sensorless Position Estimation

Jun Cai, *Senior Member, IEEE*, Yuhan Gu, Zeyuan Liu, and Shoujun Song, *Senior Member, IEEE*

***Abstract*—In this article, a cost-function extremum seeking-based model prediction torque control (CES-MPTC) method of permanent magnet synchronous motor with sensorless position estimation is proposed. First, as the predictive torque and flux linkage are the functions of the *DQ*-axis voltage components, once the partial derivative of the cost function with the *DQ*-axis voltage components are zero, the extreme point of the cost function can be located and the optimal voltage vector can be directly represented by the calculated *DQ*-axis voltage components. Using the calculated *DQ*-axis voltage components as the inputs of the space vector pulsewidth modulation module, the inverter can be controlled with fixed switching frequency as the traditional vector control. Then, an improved slide model observer-based sensorless position estimation scheme is proposed with hyperbolic sinusoidal function, frequency adaptive complex coefficient filter and quadrature phase-locked loop integrated. The sensorless position estimation scheme can be integrated with the proposed CES-MPTC, which can ensure enhanced rotor position measurement accuracy and reliable sensorless operation. Finally, detailed experimental results are provided to verify the validity of the proposed scheme.**

***Index Terms*—Cost-function extremum seeking (CES), model predictive torque control (MPTC), permanent magnet synchronous motor (PMSM), position estimation and measurement, space vector pulse width modulation (SVPWM).**

I. Introduction

PERMANENT magnet synchronous motors (PMSMs) have attracted great attentions in many industrial applications due to its significant high-power density and high control performance. The field oriented control (FOC) [1] and direct torque control (DTC) are the most popular control strategies in PMSM system. Generally, in traditional vector control, the optimization and adjustment of PI parameters are relatively complex, and their ability to resist disturbances is limited. In traditional DTC, the using of hysteresis control may result in varied switching frequencies and lowered current sinusoid degree. In view of this serious challenge, the development of a more advanced control strategy has become an extremely critical and urgent research topic [2].

In order to enhance the performance boundary of DTC, finite-control-set model predictive torque control (FCS-MPTC) has been widely explored. In FCS-MPTC, the traditional torque and flux loops are replaced with the predictive control module, which reduces the dependence on PI controllers. However, FCS-MPTC is also facing many challenges such as high computational complexity and large torque ripple [3].

At present, in-depth research has been carried out from two main dimensions. The first is to optimize the generation strategy of the control pulse to achieve finer torque and flux adjustment. The second is to explore efficient algorithms and computing architectures to reduce computational burden. In the PMSM system driven by two-level voltage source inverter, FCS-MPTC is limited by eight basic voltage vectors, and only one effective voltage vector acts on the motor [4]. This limitation results in the performance of torque and stator flux under steady-state control, manifested as significant steady-state ripple and harmonic current issues [5]. To solve this problem, some methods such as duty cycle control [6], dual vector model predictive torque control [7] and three-vector model predictive torque control (TV-MPTC) [3], [8], [9] are proposed. Compared to FCS-MPTC based on a single voltage vector, using dual vector or three vector methods can significantly improve the steady-state control quality of torque and stator flux linkage. In [6], by adjusting the duration of the voltage vector, torque fluctuations are suppressed and additional switching losses are avoided. However, the control cycle limit affects the energy efficiency of the system. In [8], by combining two virtual vectors and a zero vector, the modulation region is extended from points to line segments, thereby expanding the control range. In the control of dual PMSMs, TV-MPTC capitalizes on the motor unique stator structure, which enables the decoupling of variables into three orthogonal subspaces [3]. By determining four candidate vector groups based on torque deviation and flux position, with each group comprising two virtual vectors and one zero vector, the control

Received 1 February 2025; revised 12 April 2025 and 12 June 2025; accepted 24 June 2025. Date of publication 8 July 2025; date of current version 8 September 2025. This work was supported in part by the National Natural Science Foundation of China under Grant 52477055 and in part by Excellent Research and Innovation Teams in Universities in Anhui Province under Grant 2023AH010021. Recommended for publication by Associate Editor J. Ye. *(Corresponding author: Jun Cai.)*

Jun Cai is with the C-MEIC, CICAEET, School of Automation, Nanjing University of Information Science and Technology, Nanjing 210044, China, and also with the School of Mechanical and Electrical Engineering, Anhui Jianzhu University, Hefei 230009, China (e-mail: j.cai@nuist.edu.cn).

Yuhan Gu is with the School of Automation, Nanjing University of Information Science and Technology, Nanjing 210044, China.

Zeyuan Liu is with the School of Automation, Nanjing University of Posts and Telecommunications, Nanjing 210023, China (e-mail: liuzy@njupt.edu.cn).

Shoujun Song is with the College of Automation, Northwestern Polytechnical University, Xi'an 710072, China (e-mail: sunnyway@nwpu.edu.cn).

Color versions of one or more figures in this article are available at https://doi.org/10.1109/TPEL.2025.3586986.

Digital Object Identifier 10.1109/TPEL.2025.3586986

algorithm achieves precise control over torque and flux through duty-ratio modulation. Conversely, in [9], the TV-MPTC focuses on enhancing steady-state performance by precisely determining appropriate active voltage vectors through predicted torque error. A modified switching table, which considers only the sign of torque deviation, is employed to select active voltage vectors. This approach eliminates the need for cost function minimization enumeration, thereby improving computational efficiency. However, such methods also introduce additional calculations, especially those involving the selection of multiple voltage vectors and the precise calculation of the action time.

To alleviate the computational pressure of FCS-MPTC, in [10] and [3], a deadbeat direct torque and flux control algorithm is proposed. This method simplifies the conventional algorithm to only evaluate three voltage vectors, significantly reducing computational costs. A novel generalized hybrid method has been introduced in [11], which uses artificial neural network to train the model and directly select the optimal voltage vector, avoiding the traditional ergodic calculation. In [11], a scheme of incorporating current disturbance into adaptive fuzzy is proposed to enhance the robustness of MPC to current disturbance. This method avoids the introduction of additional controller to realize current disturbance compensation, thus reducing the complexity and calculation of the whole system. These methods reduce the search space of optimization through different mechanisms, thereby effectively reducing computational costs while maintaining high performance.

To measure accurate rotor position information is vital to implement the CES-MPTC in PMSM. Generally, the position can be acquired by sensor measurement or sensorless estimation. As compared with the sensor measurement method, the sensorless estimation scheme can ensure better environment adaptability and reduced costs [13], [14], [15], [16], [17], [18], [19], [20]. As a classical method in position sensorless technology, sliding mode observer (SMO) has strong robustness to system parameter changes and external disturbances. However, there are also shortcomings in traditional SMO, the inherent discontinuity of the controller inevitably leads to system chattering. Therefore, it is vital to improve the traditional SMO from three dimensions: improve the switching function, improve the filter and phase-locked loop (PLL). For minimize system chattering, a nonlinear saturation function was innovatively introduced as the core element of SMO in [16]. It can solve the false detection problem caused by the discontinuity of traditional SMO switching functions [17]. However, this method is susceptible to significant external interference under extreme operating conditions. To overcome these shortcomings, an SMO based on hyperbolic tangent switching function was proposed in [18]. Due to its continuous characteristics, it is possible to reduce chattering and improve the stability the observer.

The higher harmonics generated by the nonlinearity of the inverter can adversely affect the accuracy of rotor position estimation. A method that fuses a complex bandpass filter with PLL is proposed in [19]. However, there are shortcomings in frequency adaptability, phase and amplitude maintenance. Frequency adaptive complex coefficient filter (FACCF) can adaptively adjust its center frequency according to the operating speed of the motor. This enables the filter to dynamically adapt to the characteristic changes of the motor in different speed ranges, further improving the robustness and adaptability of the control system [20]. Recent advancements in PMSM harmonic suppression and rotor position estimation introduce novel observer designs addressing multi-harmonic disturbances. A master-slave observer with complex-coefficient resonators (CCRs) to decouple the back electromotive force (BEMF) is proposed in [21], which can reduce the computational load compared to real-coefficient methods while enabling selective harmonic attenuation via integrated bandpass features. However, CCR stability analysis remains complex, and low-frequency phase distortions persist. In [22], an extended state observer (ESO) in the $\gamma\delta$ frame is presented, combining resonant observers with integrated grid (ROGI) to decouple harmonics (-1st, -2nd, ± 6th orders), improving low-pass filtering and efficiency but requiring intricate frequency-domain parameterization and risking residual harmonics under dynamics. A dual-filtered complex vector observer (DCVO) with adaptive speed control is introduced in [23], achieving inherent harmonic suppression at predefined frequencies (-5th, $+7$th orders) through a minimal third-order structure. While ensuring rapid responses and stability, parameter tuning complexity and robustness limitations under wide-speed operations remain challenges.

The traditional method uses the arctangent to resolve the rotor position directly from BEMF estimate. However, when the BEMF is close to zero, it is susceptible to noise and increases the position estimation error [24]. At present, various advanced PLLs are used for more accurate rotor position acquisition in [25]. A combination of BEMF estimation based on SMO and software PLL technology is proposed in [26]. However, the performance of this method is limited when the speed direction is reversed. To avoid this problem, a nonorthogonal PLL [27] and a Q-PLL [28] are designed. Furthermore, the adaptive PLL is proposed [29] for more robust position estimation.

To improve the dynamic performance and robustness of PMSM control, a sensorless CES-MPTC strategy is proposed. The main features are as follows.

1) The optimized DQ-axis voltage components are online calculated directly by locating the extreme point of the MPTC cost function.
2) The SVPWM module is used to control the PMSM at a fixed switching frequency. As compared to traditional vector control, the two inner PI controllers are avoided. As compared with the traditional FCS-MPTC, the overall computation burden can be highly alleviated.
3) The three methods of hyperbolic tangent function, FACCF and orthogonal PLL are integrated to solve the problems existing in traditional SMO. As a result, the accuracy and dynamic performance of position estimation can be improved.

The rest of this article is organized as follows: In Section II, the principle of the proposed sensorless CES-MPTC is presented. In Section III, the experimental results are discussed in detail. Finally, Section IV concludes this article.

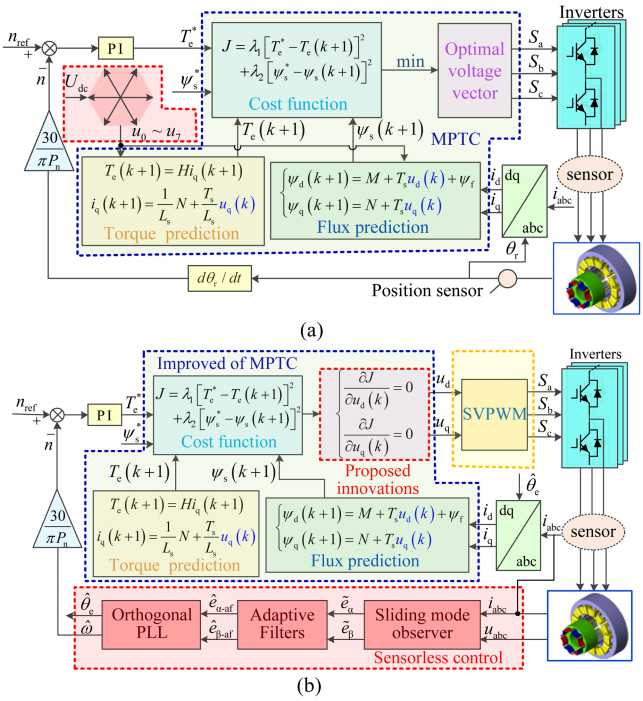

Fig. 1. Control block diagrams of two MPTC strategies. (a) Traditional FCS-MPTC. (b) Proposed sensorless CES-MPTC.

II. Principle of the Proposed Sensorless CES-MPTC

A. Motivation of the Development of the Proposed Scheme

The core of traditional direct torque control strategy lies in constructing a dual closed-loop feedback mechanism of torque and magnetic flux, and cleverly integrating proportional integral (PI) controller to ensure the stability and reliability of system operation. However, the PI controller has the following issues.

1) While stabilizing system performance, the agility of system dynamic response is inevitably sacrificed.
2) The inherent limitations of PI controllers, such as the nondynamic adjustability of parameters, which limits the ability to cope with external conditions such as motor load fluctuations, environmental temperature fluctuations, and power supply instability.
3) When facing rapid load changes or external disturbances, PI controllers are prone to overshoot and oscillation phenomena.

To overcome the above challenges, as shown in Fig. 1(a), introducing MPC into the torque control loop has become an innovative strategy. This method can improve the adaptability of the system to complex working conditions with fast responses. However, in practical applications, there is a core challenge: it is necessary to undergo up to seven iterative calculations within each control cycle to accurately select the optimal voltage vector. This intensive computing demand puts significant pressure on the controller. Furthermore, due to the nonfixed frequency of voltage vector selection, significant fluctuations in magnetic flux and torque may exist.

As shown in Fig. 1(b), a new method based on the derivative of the cost function is proposed. This method utilizes the partial derivative information of the cost function on the voltage vector to directly calculate the components of the optimal voltage vector in the DQ coordinate system. Furthermore, this method can be seamlessly integrated with SVPWM technology. In addition, the improved SMO-based sensorless methods can be combined with the proposed method to ensure reliable position estimation, which can further reduce the cost of the system while improving its reliability and robustness. Based on the above analysis, it can be concluded that the proposed sensorless CES-MPTC has the following advantages.

1) CES-MPTC uniquely computes the optimal voltage vector by directly solving the extremum of the cost function, eliminating the need for exhaustive search algorithms used in traditional methods, thereby significantly reducing computational burden. This scheme is more suitable for low-cost embedded controllers with improved real-time control performance.
2) By integrating SVPWM, CES-MPTC maintains a fixed switching frequency, which enhances torque and flux ripple suppression, improving system stability and accuracy compared to traditional MPTC methods with variable switching frequencies. By eliminating the two internal PI controllers in traditional FOC and achieving fixed switching frequency, CES-MPTC exhibits faster dynamic response and enhanced robustness under load disturbances and speed variations
3) CES-MPTC incorporates an improved SMO with hyperbolic tangent switching function, FACCF, and orthogonal PLL, enabling more accurate and robust rotor position estimation without position sensors.

B. Principle of the Proposed CES-MPTC

1) Basic Model of the PMSM: For a surface-mounted PMSM, the stator voltage equation can be expressed as

$$\begin{cases} u_d = Ri_d + \frac{d\psi_d}{dt} - \omega\psi_q \\ u_q = Ri_q + \frac{d\psi_q}{dt} + \omega\psi_d \end{cases} \tag{1}$$

where R is the stator winding; i_d, i_q are the DQ-axis current component; ω is rotor angular velocity; ψ_d,ψ_q are the DQ-axis stator magnetic flux components, which can be expressed as

$$\begin{cases} \psi_d = L_d i_d + \psi_f \\ \psi_q = L_q i_q \end{cases} \tag{2}$$

where $L_d = L_q = L_s$ are the stator winding inductance and ψ_f is permanent magnet flux;

The stator magnetic flux can be expressed by

$$\psi_s = \sqrt{\psi_d^2 + \psi_q^2}. \tag{3}$$

For surface-mounted PMSM, the torque equation is relatively is expressed as

$$T_e = \frac{3}{2} P_n \psi_f i_q \tag{4}$$

where P_n is the number of motor pole pairs.

2) Basic Model of Predicted Torque and Flux Linkage: The differential equation expression of PMSM current in a rotating

coordinate system can be expressed as

$$\begin{bmatrix} \frac{di_d}{dt} \\ \frac{di_q}{dt} \end{bmatrix} = \begin{bmatrix} -\frac{R}{L_s} & \omega \\ \omega & -\frac{R}{L_s} \end{bmatrix} \begin{bmatrix} i_d \\ i_q \end{bmatrix} + \begin{bmatrix} \frac{1}{L_s} u_d \\ \frac{1}{L_s} u_q - \omega \frac{\psi_f}{L_s} \end{bmatrix}. \quad (5)$$

Using the first-order Euler discretization formula to discretize the current differential equation, the DQ-axis currents at time $k+1$ are expressed as

$$\begin{cases} i_d(k+1) = \frac{1}{L_s} M + \frac{T_s}{L_s} u_d(k) \\ i_q(k+1) = \frac{1}{L_s} N + \frac{T_s}{L_s} u_q(k) \end{cases} \quad (6)$$

where M and N are intermediate variables, represented as

$$\begin{cases} M = (L_s - RT_s) i_d(k) + \omega T_s L_s i_q(k) \\ N = (L_s - RT_s) i_q(k) - \omega T_s L_s i_d(k) - \psi_f \omega T_s \end{cases}. \quad (7)$$

The predicted torque value for the next instant can be expressed as

$$T_e(k+1) = \frac{3}{2} P_n \psi_f i_q(k+1). \quad (8)$$

The predicted magnetic flux value at the next instant is

$$\begin{cases} \psi_d(k+1) = L_d i_d(k+1) + \psi_f \\ \psi_q(k+1) = L_q i_q(k+1) \end{cases}. \quad (9)$$

Based on (5) and (9), the predicted magnetic flux can be expressed as

$$\begin{cases} \psi_d(k+1) = M + T_s u_d(k) + \psi_f \\ \psi_q(k+1) = N + T_s u_q(k) \end{cases}. \quad (10)$$

The core of the traditional FCS-MPTC strategy is to use stator magnetic flux and electromagnetic torque as key control variables. To ensure a balanced consideration of both during the optimization process, the cost function J in the form of a weighted sum of stator flux error and electromagnetic torque error is utilized, which is expressed as

$$J = \lambda_1 [T_e^* - T_e(k+1)]^2 + \lambda_2 [\psi_s^* - \psi_s(k+1)]^2 \quad (11)$$

where T_e^* and ψ_s^* are the reference values for torque and stator magnetic flux, respectively; λ_1,λ_2 is the weight coefficient. The weight coefficient in this article is selected through a large number of experiments, taking λ_1:λ_2 = 1:20.

3) Calculation of U_d *and* u_q*:* Based on the above analysis, it can be concluded that the voltage vector that minimizes the cost function is the optimal voltage vector. Combining (4) and (7), it can be concluded that torque is only related to the Q-axis current; It was found from (6) that it is only related to the Q-axis voltage. Similarly, combining (3) and (9), it can be concluded that the magnetic flux is related to the DQ-axis current, that is, to the DQ-axis voltage.

Therefore, by taking the derivative of the cost function and making it equal to 0, the cost function can be minimized. Fig. 2 provides a more intuitive representation of the logical relationship in the calculation process of voltage vectors. The derivative

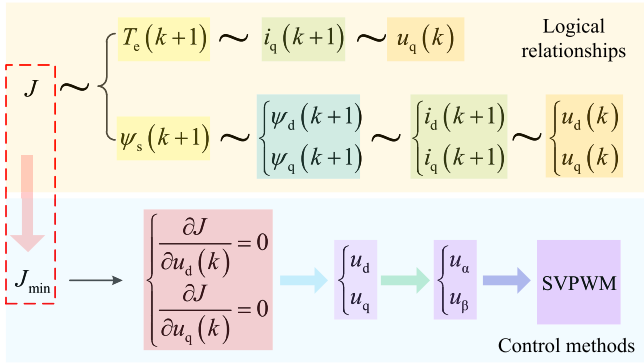

Fig. 2. Diagram of derivative solution logic analysis.

of the cost function on $u_d(k)$ and $u_q(k)$ can be expressed as

$$\begin{cases} \frac{\partial J}{\partial u_d(k)} = \frac{\partial \left[\lambda_2 \left(\psi_d^2 - 2\psi_d \psi_d(k+1) + \psi_d^2(k+1)\right)\right]}{\partial u_d(k)} \\ \frac{\partial J}{\partial u_q(k)} = \frac{\partial \left[\lambda_1 \left((T_e^*)^2 - 2T_e^* T_e(k+1) + T_e^2(k+1)\right)\right]}{\partial u_q(k)} \\ \qquad + \frac{\partial \left[\lambda_2 \left(\psi_q^2 - 2\psi_q \psi_q(k+1) + \psi_q^2(k+1)\right)\right]}{\partial u_q(k)} \end{cases}. \quad (12)$$

Then, make the partial derivative equal to 0, expressed as

$$\begin{cases} \frac{\partial J}{\partial u_d(k)} = 0 \\ \frac{\partial J}{\partial u_q(k)} = 0 \end{cases}. \quad (13)$$

Thus, the $u_d(k)$ and $u_q(k)$ values corresponding to the minimum cost function can be obtained as

$$\begin{cases} u_d(k) = \frac{\psi_d - M - \psi_f}{T_s} \\ u_q(k) = \frac{\frac{\lambda_1 H}{L_s} T_e^* + \lambda_2 \psi_q - \left(\lambda_1 \frac{H^2}{L_s^2} + \lambda_2\right) N}{T_s \left(\lambda_1 \frac{H^2}{L_s^2} + \lambda_2\right)} \end{cases} \quad (14)$$

where $H = 3/2 P_n \psi_f$.

C. Sensorless Position Estimation Scheme

Based on the aforementioned analysis, CES-MPTC is designed to utilize SVPWM technology for the inversion process, with its switching frequency being fixed. During one output cycle, the three-phase voltages are controlled to synthesize a voltage vector, which is achieved through the implementation of SVPWM technology. Consequently, the magnetic field inside the motor rotates at a constant angular velocity, resulting in the formation of a circular flux trajectory. Therefore, like the traditional field-oriented control, most of those traditional sensorless position estimation schemes can also be utilized and combined with the proposed CES-MPTC method. In this article, an improved SMO-based sensorless method is developed to combine with the CES-MPTC method.

Aiming at the phenomenon that oscillation and instability may occur in the traditional SMO, the improvements are mainly made from three aspects: the optimization of the symbol function, the improvement of LPF and the rotor position estimation strategy.

The traditional SMO is a nonlinear observer designed based on current measurement and current error, which reconstructs

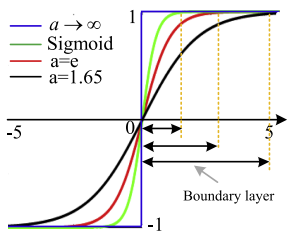

Fig. 3. Schematic diagram of improved hyperbolic tangent function.

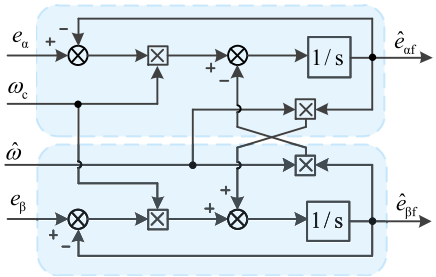

Fig. 4. Structural diagram of FACCF.

the BEMF using current error. Based on the current state equation on the $\alpha\beta$-axis, the surface of SMO can be designed based on the current observation error. The dynamic current error equation can be expressed as

$$\frac{d}{dt}\begin{bmatrix}\tilde{i}_\alpha\\ \tilde{i}_\beta\end{bmatrix} = -\frac{R}{L_s}\begin{bmatrix}\tilde{i}_\alpha\\ \tilde{i}_\beta\end{bmatrix} + \frac{1}{L_s}\begin{bmatrix}u_\alpha\\ u_\beta\end{bmatrix} - \frac{1}{L_s}\begin{bmatrix}e_\alpha - v_\alpha\\ e_\beta - v_\beta\end{bmatrix} \tag{15}$$

where $\tilde{i}_\alpha$, $\tilde{i}_\beta$ are the current observation error; v_α, v_β represents the estimated BEMF; e_α, e_β represents the extended BEMF

$$\begin{cases} e_\alpha = -\omega\psi_f \sin\theta_e \\ e_\beta = \omega\psi_f \cos\theta_e \end{cases} \tag{16}$$

where θ_e is the rotor electrical angle.

To further minimize the chattering effects, the hyperbolic tangent function is utilized [18]. The expression of hyperbolic tangent function is

$$f(x) = \frac{a^x - a^{-x}}{a^x + a^{-x}}. \tag{17}$$

As illustrated in Fig. 3, the hyperbolic tangent function is continuously differentiable near the zero point, which can smooth the transition switching process and effectively suppress high-frequency chattering. In addition, a as parameter controls the slope of the function. The larger the value of a, the higher the slope of the function near zero, and the faster the dynamic response, but it may cause small amplitude oscillation. Reducing the value of a can enhance the antinoise ability, but the response speed is reduced. Finally, after a large number of experiments, $a = 2.2$ was selected as the optimal parameter, taking into account the response speed and antinoise performance.

For further reducing the chattering phenomenon and eliminate phase shift, the FACCF as illustrated in Fig. 4 is also adopted [20]. In the process of estimating the BEMF, the center frequency of FACCF will be dynamically adjusted according to the motor speed estimated by SMO. By adapting to the real-time change of motor running state, no amplitude attenuation and phase offset can be realized. LPF has unity gain and no delay at zero frequency. If the center frequency of LPF is moved to ω_0 in the frequency domain, the complex coefficient filter (CCF) is

$$\mathrm{CCF}(s - j\omega_0) = \frac{\omega_c}{s - j\omega_0 + \omega_c} \tag{18}$$

where ω_0 and ω_c are the center frequency and bandwidth frequency respectively. By selecting the center frequency of CCF as the frequency of the BEMF, and using the estimated angular velocity of the motor as the center frequency, the filtered BEMF can be represented as

$$\begin{bmatrix}\hat{e}_{\alpha f}\\ \hat{e}_{\beta f}\end{bmatrix} = \frac{\omega_c}{s+\omega_c}\begin{bmatrix}\tilde{e}_\alpha\\ \tilde{e}_\beta\end{bmatrix} + \frac{\hat{\omega}}{s+\omega_c}\begin{bmatrix}-\hat{e}_{\beta f}\\ \hat{e}_{\alpha f}\end{bmatrix} \tag{19}$$

where $\tilde{e}_\alpha$ and $\tilde{e}_\beta$ are the estimated BEMF after the switching function; $\hat{e}_{\alpha f}$ and $\hat{e}_{\beta f}$ are the estimated BEMF after filtering. When designing FACCF, it should ensure that its center frequency matches the estimated electrical angular velocity, and the cut-off frequency changes adaptively with the estimated electrical angular velocity in real-time.

$$\begin{cases} \omega_0 = \hat{\omega} \\ \omega_c = k_c\hat{\omega} \end{cases} \tag{20}$$

where $\hat{\omega}$ is the estimated electrical angular velocity, and k_c is the cut-off frequency coefficient. The bandwidth characteristic of FACCF is directly affected by k_c. Through a large number of experiments, the value of k_c is 1.

TABLE I
COMPARISON OF DIFFERENT FILTERS

Method	Harmonic suppression	Parameter complexity	Dynamic response	Computational efficiency
FACCF [18]	Adaptive Multi-harmonic	Low	Fast	High
CCR [19]	Multi-harmonic separation	High	Medium	Low
ESO [20]	± 6th harmonic	High	Medium	Low
DCVO [21]	-5/+7 harmonics	High	Slow	Medium

A comparison of different filters is illustrated in Table I. As shown in this table, FACCF demonstrates clear superiority over prior strategies through frequency adaptability, ensuring zero phase lag and amplitude preservation, whereas the master-slave architectures, ROGI, and DCVO may introduce implementation complexities, computational burdens, or stability challenges. Compared with the degradation of ESO, incomplete harmonic suppression of ROGI, and sluggish dynamics of DCVO, the filtering performance of FACCF can achieve zero phase distortion of the center frequency and robust harmonic suppression at low carrier ratios. Unlike the multi-gain tuning of CCR or the complex coefficient stability issues of ESO, the parameter configuration of FACCF is simplified by only requiring a cut-off frequency specification.

Finally, an orthogonal PLL as illustrated in Fig. 5 is adopted to calculate the rotor position. The orthogonal PLL can naturally eliminate the velocity information contained in the BEMF through trigonometric transformation. Due to the variation of BEMF with speed, the BEMF of PLL tracking estimator is

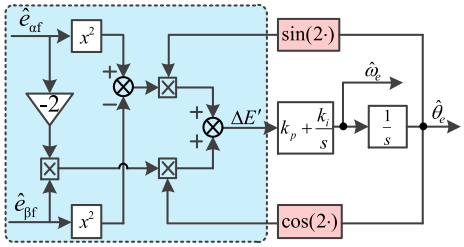

Fig. 5. Schematic diagram of improved orthogonal PLL.

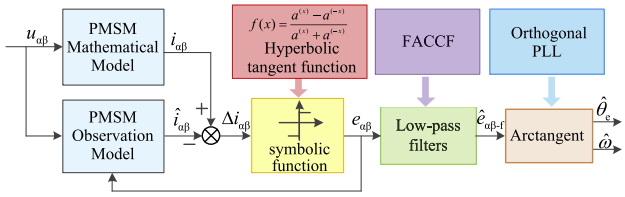

Fig. 6. Block diagram of the proposed sensorless position estimation scheme.

normalized [28]. The normalized position error signal can be expressed as

$$\Delta E_1' = -2\hat{e}_{\alpha f}\hat{e}_{\beta f}\cos(2\hat{\theta}_e) + \left(\hat{e}_{\beta f}^2 - \hat{e}_{\alpha f}^2\right)\sin(2\hat{\theta}_e). \quad (21)$$

Therefore, the rotor position estimation obtained from the proposed PLL can be expressed as

$$\hat{\theta}_e = \frac{k_p s + k_i}{s^2}\Delta E_1'. \quad (22)$$

1) The overall control block diagram of the improved SMO-based position estimation method is shown in Fig. 6 The following possible advantages can be achieved. The adoption of an improved hyperbolic tangent function can fundamentally eliminate the mutation points in traditional sign function. Thus, the high-frequency chattering phenomenon generated during the dynamic process of sliding mode can be reduced.
2) The FACCF is adopted to replace the low-pass filter, which can accurately identify and eliminate harmonic interference. Thus, the accuracy of rotor position and speed estimation can be significantly improved.
3) An improved orthogonal PLL is utilized to replace the Arctangent function. Due to its excellent tracking performance and fast response capability, accurate and efficient rotor position estimation can be achieved.

III. Experimental Results

To verify the validity of the proposed control strategies, the experiments have been performed on a two PMSMs towing system. As shown in Fig. 7, one motor is used as a propulsion motor and the other one is a loading generator. The rated parameter of the tested PMSM prototype is rated 24V/60W/3000rpm, and the specific parameters of the motor are given in Table II. The overall control block diagram of the proposed sensorless MPTC

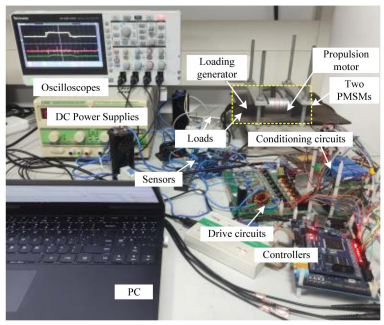

Fig. 7. Test-bed system.

TABLE II
Specifications of the Tested Motor

Parameters	Value
Phase resistor (Ω)	0.6
Phase inductance (mH)	1.1
Power rating (W)	60
Current rating (A)	3.3
Voltage rating (V)	24
Rated torque(N·m)	0.18

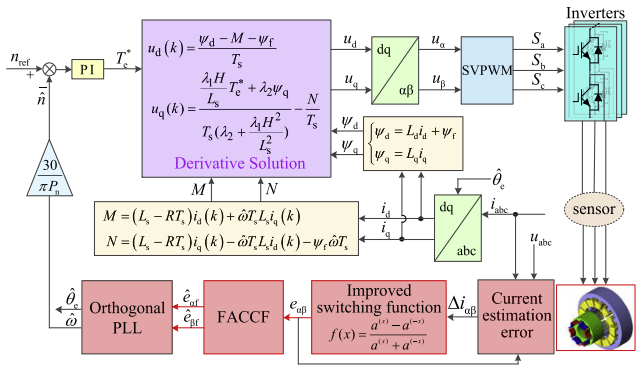

Fig. 8. Based on the improved CES-MPTC sensorless system diagram.

is shown in Fig. 8 and the overall algorithms are all implemented in a TMS320F28335-based controller.

To demonstrate the superiority of the proposed sensorless CES-MPTC performance, experiments are conducted via the following three aspects.

1) The effectiveness of CES-MPTC is validated and compared with traditional FCS-MPTC and FOC control strategies.
2) The superiority of the improved SMO-based sensorless position estimation scheme is verified by four different combination modes.
3) The validity of the sensorless CES-MPTC is also verified.

A. Experimental Results of the CES-MPTC Under Steady-State Operation and Dynamic Operation

The steady-state control performance of different control strategies at 1000 rpm is shown in Figs. 9 and 10. As shown

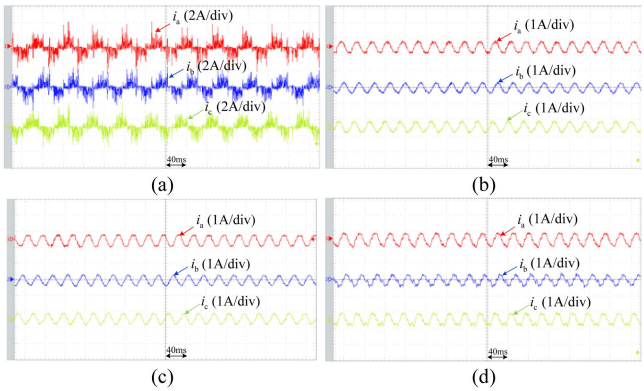

Fig. 9. Waveform of three-phase current under different methods. (a) Finite-control-set model predictive torque control. (b) Field oriented control. (c) Three-vector model predictive torque control. (d) Cost-function extremum seeking-based model prediction torque control.

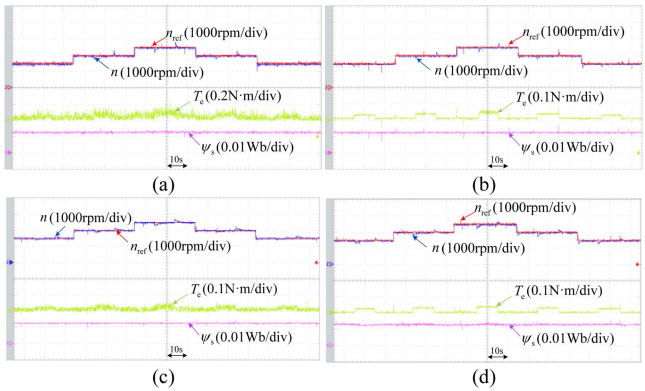

Fig. 11. Dynamic waveform under different methods. (a) Finite-control-set model predictive torque control. (b) Field oriented control. (c) Three-vector model predictive torque control. (d) Cost-function extremum seeking-based model prediction torque control.

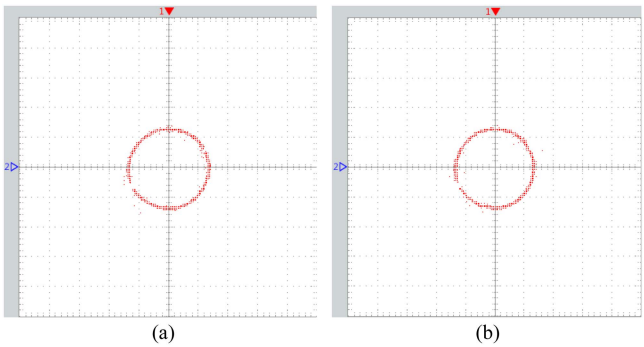

Fig. 10. Stator flux trajectory under 1000 r/min. (a) Field oriented control. (b) Cost-function extremum seeking-based model prediction torque control.

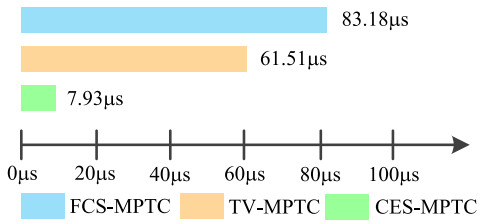

Fig. 12. Time diagrams for three types of torque control operation.

in Fig. 9(a), the traditional single vector FCS-MTPC only uses one effective voltage vector in each control cycle, and the switching frequency is not fixed, resulting in high harmonic content in the current. In Fig. 9(c), TV-MPTC achieves a nearly constant switching frequency by calculating the duty cycle [9]. Consequently, the system stability is enhanced. As can be seen in Fig. 9(b) and (c), as the SVPWM strategy is utilized in FOC and the proposed CES-MPTC, the switching frequency of inverter can be fixed, thereby the harmonics in phase current can be highly eliminated. Compared with FOC, the proposed CES-MPTC can avoid using two PI controllers in the two current loops while still maintaining high stability in steady-state operation.

In Fig. 10(a) and (b), it can be clearly seen that under the control of CES-MPTC, the trajectory of stator magnetic flux exhibits a circular characteristic. Therefore, the magnetic field state of the motor is evenly distributed in space, and the magnetic flux in the stator winding changes smoothly. Therefore, it is conducive to generating continuous sinusoid back-emf, which can help improving the rotor position estimation accuracy.

To validate the dynamic operational effectiveness of CES-MPTC, tests were conducted on the speed closed-loop transition processes with various reference speeds. Under conditions of sudden speed changes and load variations, the rotor speed was capable of promptly tracking the reference values. As discussed in Fig. 11(a), only a limited number of voltage vectors are selectable for each control cycle, with their amplitude and direction being fixed. This limitation may result in the system being unable to fully meet the current control demands during voltage vector selection, leading to significant torque and flux ripple. In Fig. 11(b), the FOC achieved precise regulation of motor performance by decoupling torque and magnetization control. However, as two inner PI control loops exist, complex PI parameters tuning process is required and the dynamic responses of the controller are affected. As illustrated in Fig. 11(c), TV-MPTC reduces torque ripple under single-vector operation by synthesizing multiple vectors. However, since this method is still based on voltage vectors in the discrete domain, it exhibits relatively large torque ripple compared to vector control. As shown in Fig. 11(d), compared with the other three control strategies, the CES-MPTC can ensure smoother torque tracking and high-speed dynamic response. Compared with the FOC method, the two inner PI control loops are eliminated, and there is no need for a complex PI parameter tuning process. The controller can still easily achieve good dynamic response and lower torque ripple.

Subsequently, the computational burdens of three torque control schemes were compared. In the DSP28335 controller, the execution time, which serves as a metric for computational complexity, can be directly read from the console. The execution times depicted in Fig. 12 represent the duration from vector calculation to the determination of the optimal voltage vector within one cycle for different control strategies. Notably, for

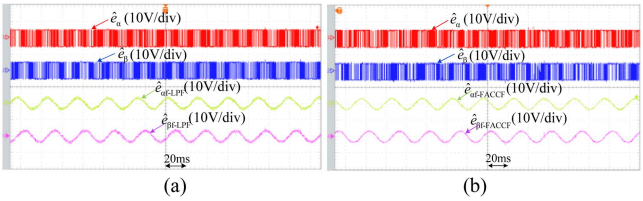

Fig. 13. BEMF before and after filtering. (a) Mode I. (b) Mode II.

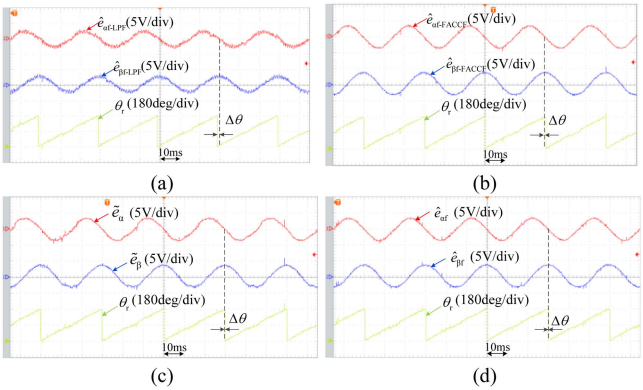

Fig. 14. Estimated BEMF and rotor position under different operation modes. (a) Mode I. (b) Mode II. (c) Mode III. (d) Mode IV.

TV-MPTC, this time also includes the duration for duty cycle calculation. The experimental results reveal that the execution times for the three control schemes are 83.18, 61.51, and 7.93 μs, respectively. It can thus be inferred that the proposed CES-MPTC significantly reduces the computational complexity of the system.

B. Experimental Results of the Improved SMO-Based Position Estimation Method

To verify the validity of proposed sensorless position estimation scheme, the following four operation modes were selected for comparison in this experiment.

1) *Mode* I: Traditional SMO with LPF.
2) *Mode* II: Traditional SMO with FACCF.
3) *Mode* III: Improved SMO (with hyperbolic tangent function).
4) *Mode* IV: Improved SMO with FACCF. In the four modes, the rotor positions are finally calculated with the orthogonal PLL.

As shown in Fig. 13(a), due to charting effects in the traditional SMO, it is vital to add a filter to obtain the BEMF. However, when using LPF, it is inevitable to introduce some side effects such as phase distortion and signal delay. To overcome this problem, the FACCF can be adopted. As shown in Fig. 13(b), the high frequency harmonics can be eliminated much better than that in operation mode I.

The position estimation results of the four operation modes are compared, which are shown in Figs. 14, 15, and 16. As shown in Fig. 14(a), the using of LPF introduces amplitude attenuation and phase shift in the estimated rotor position. As can be seen in Fig. 14(b), compared to mode I, the FACCF

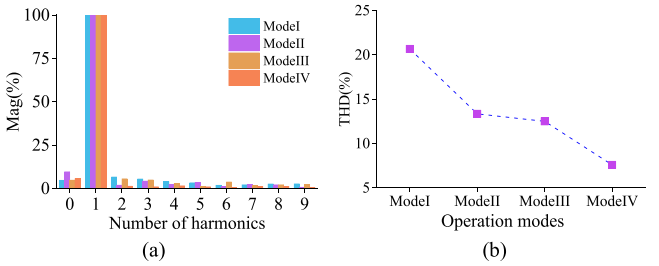

Fig. 15. Comparison of the FFT results of the estimated BEMF in the four operation modes. (a) FFT results. (b) THD of the BEMF in the four modes.

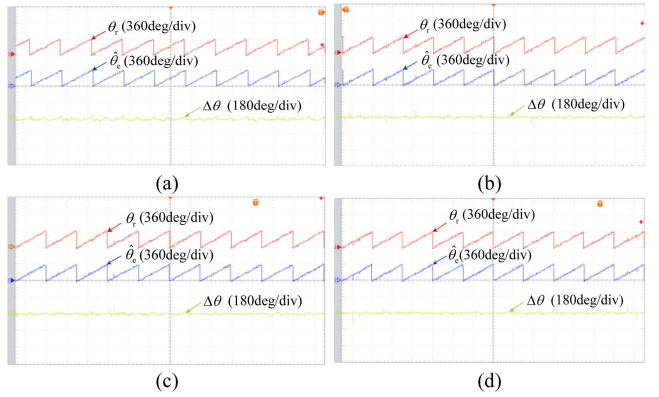

Fig. 16. Estimation angle and actual angle error waveform in four modes. (a) Mode I. (b) Mode II. (c) Mode III. (d) Mode IV.

utilized in mode II can maintain signal authenticity and integrity by automatically adjusting the center frequency with rotational speed. In mode III, by using the hyperbolic tangent function as the switching function of the SMO, the BEMF can be estimated without LPF. However, the estimated BEMF signals are distorted so that more high-order harmonics will be introduced. As illustrated in Fig. 14(d), in mode IV, by adding the FACCF, the sinusoidal degree of the estimated BEMF can be further improved. In addition, compared with Mode I, the phase shift of the BEMF obtained by other three methods was well suppressed.

The total harmonic distortion (THD) of the estimated BEMF under the four operation modes are compared in Fig. 15(a). As can be seen in Fig. 15(b), the THD of BEMF in mode I is the highest, which reaches about 20.68%. In mode II and mode III, the THD of BEMF is decreased to 13.36% and 12.51%, respectively. In mode IV, the lowest of the THD of the four modes can be achieved, which is about 7.6%. Therefore, the integration of hyperbolic tangent function and FACCF can ensure better sinusoid degree of the estimated BEMF. The tested position estimation results of the four modes are also compared in Fig. 16. Compared with traditional SMO, this strategy reduces the rotor position estimation error by 75%, with a position error of about 1.5°. The result not only demonstrates its excellent ability to improve system stability, but also deeply validates the effectiveness and practicality of the proposed method in improving the position estimation accuracy.

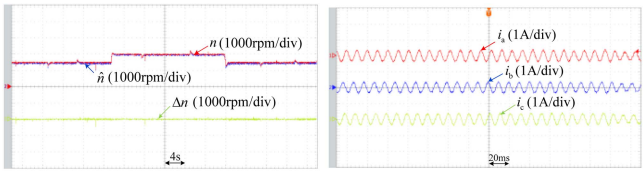

Fig. 17. Tested waveforms of the proposed sensorless CES-MPTC. (a) Speed waveform under dynamic operations. (b) Three phase current at steady state.

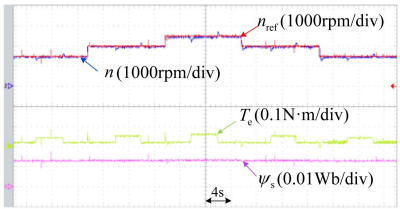

Fig. 18. Dynamic waveform under variable speed and load transitions.

C. Experimental Results of the Sensorless CES-MPTC Scheme

The steady state and dynamic driving operation of the proposed sensorless CES-MPTC is also tested for verification. As shown in Fig. 17(a), it can be clearly observed that the estimated speed can accurately track the actual speed value under dynamic operation conditions with speed transitions and load transitions. The experimental results show that even under the influence of speed changes and load disturbances, the motor drive system can operate stably in sensorless operation. The waveform of three-phase current in steady state operation is also shown in Fig. 17(b). Due to the fixed switching frequency of the proposed sensorless CES-MPTC strategies, the three-phase current can be smoothly with higher sinusoid degree compared to traditional FCS-MPTC methods.

The torque and flux linkage under dynamic speed and load conditions are shown in Fig. 18. As can be seen in this figure, when introducing a load disturbance, the torque responds almost immediately with a significant increase, which ensures the speed can quickly recover to the required level. On the contrary, when the disturbance is eliminated, the torque can quickly decrease to an appropriate level, reflecting the high flexibility and accuracy of the torque control mechanism. It is worth noting that at the moment when the speed undergoes a step change, the torque also shows a corresponding dynamic adjustment. This phenomenon highlighted the fast response capability of the torque control system in dealing with sudden signals and its effectiveness under high dynamic performance requirements.

IV. Conclusion

In this article, a CES-MPTC control strategy for PMSM with sensorless position estimation is proposed for the PMSM drive system. Detailed theoretical analysis and experimental results are discussed for verification. The main features of this article are as follows.

1) Introducing MPC into the traditional torque control field avoids the adverse effects of the inherent limitations of PI controllers. This in turn improves the dynamic response of the system.
2) The optimal voltage vector is directly obtained by calculating the partial derivative of the cost function of the MPTC, which greatly reduces the computational burden of FCS-MPTC. Furthermore, as the switching frequency can be fixed under SVPWM control, the fluctuations in magnetic flux and torque can be better suppressed. In turn, the real-time control performance of the system can be improved.
3) Accurate rotor position is highly required in the PMSM control system. To eliminate dependence on position sensors and enhance the overall reliability of the position measurement process, the sensorless position estimation scheme is also developed in this article. Like the traditional FOC strategy, all the traditional and improved sensorless position estimation strategies can also be integrated with the proposed CES-MPTC. In this article, the improved SMO with integrated hyperbolic tangent function, FACCF and orthogonal PLL enables more accurate estimation of rotor position information. Experimental results show that the sensorless CES-MPTC strategy can operate stably with high robustness even under speed changes and load disturbance.

References

[1] Z. Wu, Z. Yang, K. Ding, and G. He, "Transfer mechanism analysis of injected voltage harmonic and its effect on current harmonic regulation in FOC PMSM," *IEEE Trans. Power Electron.*, vol. 37, no. 1, pp. 820–829, Jan. 2022.
[2] E. Zerdali, M. Rivera, and P. Wheeler, "A review on weighting factor design of finite control set model predictive control strategies for AC electric drives," *IEEE Trans. Power Electron.*, vol. 39, no. 8, pp. 9967–9981, Aug. 2024.
[3] Y. Liu et al., "Three-vector-based model predictive torque control for dual three-phase PMSM with torque and flux ripples reduction," *IEEE Trans. Power Electron.*, vol. 39, no. 8, pp. 10009–10020, Aug. 2024.
[4] F. Wang, Z. Chen, P. Stolze, J.-F. Stumper, J. Rodríguez, and R. Kennel, "Encoderless finite-state predictive torque control for induction machine with a compensated MRAS," *IEEE Trans. Ind. Inform.*, vol. 10, no. 2, pp. 1097–1106, May 2014.
[5] C. Zhou, H. Li, L. Yang, R. Liu, and B. Chen, "Low complexity zero-suboptimal model predictive torque control for SPMSM drives based on discrete space vector modulation," *IEEE J. Emerg. Sel. Topics Power Electron.*, vol. 12, no. 4, pp. 4204–4215, Aug. 2024.
[6] Z. Song, X. Ma, and R. Zhang, "Enhanced finite-control-set model predictive flux control of permanent magnet synchronous machines with minimum torque ripples," *IEEE Trans. Ind. Electron.*, vol. 68, no. 9, pp. 7804–7813, Sep. 2021.
[7] Y. Zhang and H. Yang, "Generalized two-vector-based model-predictive torque control of induction motor drives," *IEEE Trans. Power Electron.*, vol. 30, no. 7, pp. 3818–3829, Jul. 2015.
[8] K. Yu, Z. Wang, W. Hua, and M. Cheng, "Robust cascaded deadbeat predictive control for dual three-phase variable-flux PMSM considering intrinsic delay in speed loop," *IEEE Trans. Ind. Electron.*, vol. 69, no. 12, pp. 12107–12118, Dec. 2022.
[9] X. Li, Z. Xue, L. Zhang, and W. Hua, "A low-complexity three-vector-based model predictive torque control for SPMSM," *IEEE Trans. Power Electron.*, vol. 36, no. 11, pp. 13002–13012, Nov. 2021.
[10] W. Wang, C. Liu, S. Liu, and H. Zhao, "Model predictive torque control for dual three-phase PMSMs with simplified deadbeat solution and discrete space-vector modulation," *IEEE Trans. Energy Convers.*, vol. 36, no. 2, pp. 1491–1499, Jun. 2021.

[11] H. A. G. Al-kaf, L. M. Halabi, and K.-B. Lee, "A generalized integrated MPC-fuzzy-neural network approach for multilevel inverter Fed PMSMs," *IEEE Trans. Ind. Inform.*, vol. 20, no. 2, pp. 2751–2761, Feb. 2024.
[12] S. Zhang, A. Shen, X. Luo, Q. Tang, and Z. Li, "An adaptive strategy for PMSM-based disturbance estimation and online parameter identification," *IEEE/ASME Trans. Mechatron.*, vol. 29, no. 4, pp. 2522–2533, Aug. 2024.
[13] S. Xu, L. Tao, C. Liu, and G. Han, "A cost-effective phase current sensing scheme involving online error correction for switched reluctance motor drive," *IEEE Trans. Instrum. Meas.*, vol. 72, 2023, Art. no. 1010111.
[14] G. Han, Z. Lu, M. Wu, S. Xu, and B. Zhu, "Improved position estimation method for SRM considering current measurement errors," *IEEE Trans. Instrum. Meas.*, vol. 71, 2022, Art. no. 9509910.
[15] A. Rolán, E. Romero-Ramírez, S. Bogarra, and J. Saura, "Speed estimation in PMSG-based wind turbines from DC voltage measurement," *IEEE Trans. Instrum. Meas.*, vol. 73, 2024, Art. no. 9005613.
[16] P. Luo, Z. Yin, Z. Zhang, Y. Zhang, P. Zhang, and J. Liu, "Diversified diagnosis strategy for PMSM inter-turn short-circuit fault via novel sliding mode observer," *IEEE Trans. Power Electron.*, vol. 39, no. 4, pp. 4149–4159, Apr. 2024.
[17] H. Hamad Boughezala, K. Laroussi, S. Khadar, A. S. Al-Sumaiti, and M. A. Mossa, "Optimized sensorless control of five-phase permanent magnet synchronous motor using a genetic algorithm-real time implementation," *IEEE Access*, vol. 12, pp. 98367–98378, 2024.
[18] P. Zhang, Z. Y. Shi, J. C. Lin, B. Yu, Y. Q. Sun, and H. Y. Ding, "Improved sensorless vector control system for permanent magnet synchronous motors based on hyperbolic tangent functions," *J. Harbin Inst. Technol.*, vol. 42, no. 5, 2021, Art. no. 9.
[19] Z. Yin, Y. Zhang, X. Cao, D. Yuan, and J. Liu, "Estimated position error suppression using novel PLL for IPMSM sensorless drives based on full-order SMO," *IEEE Trans. Power Electron.*, vol. 37, no. 4, pp. 4463–4474, Apr. 2022.
[20] Q. An, J. Zhang, Q. An, X. Liu, A. Shamekov, and K. Bi, "Frequency-adaptive complex-coefficient filter-based enhanced sliding mode observer for sensorless control of permanent magnet synchronous motor drives," *IEEE Trans. Ind. Appl.*, vol. 56, no. 1, pp. 335–343, Jan./Feb. 2020.
[21] B. Wang, P. Du, M. Tian, and D. Xu, "A master-slave-structure position observer for multiharmonics suppression in sensorless PMSM drives," *IEEE Trans. Ind. Electron.*, vol. 71, no. 5, pp. 4528–4540, May 2024.
[22] P. Du, B. Wang, and D. Xu, "A BEMF harmonic-extended state $\gamma\delta$-axes observer for PMSM sensorless control reducing structural redundancy," *IEEE Trans. Ind. Electron.*, vol. 72, no. 5, pp. 4623–4638, May 2025.
[23] G. Wang, X. Yi, and H. Lin, "A dual-filtering complex vector observer for harmonic suppression in sensorless PMSM drivers," *IEEE Trans. Power Electron.*, vol. 40, no. 5, pp. 6643–6652, May 2025.
[24] S. Chen, W. Ding, R. Hu, X. Wu, and S. Shi, "Sensorless control of PMSM drives using reduced order quasi resonant-based ESO and newton–raphson method-based PLL," *IEEE Trans. Power Electron.*, vol. 38, no. 1, pp. 229–244, Jan. 2023.
[25] J. Cai, Y. Gu, A. David Cheok, and Y. Yan, "A survey of phase-locked loop technologies in sensorless position estimation of permanent magnet synchronous motor drives," *IEEE Trans. Instrum. Meas.*, vol. 73, 2024, Art. no. 1504016.
[26] G. Zhang, G. Wang, D. Xu, and N. Zhao, "ADALINE-network-based PLL for position sensorless interior permanent magnet synchronous motor drives," *IEEE Trans. Power Electron.*, vol. 31, no. 2, pp. 1450–1460, Feb. 2016.
[27] J. Xu, Y. Du, H. Fang, H. Guo, and Y.-H. Chen, "A robust observer and nonorthogonal PLL-based sensorless control for fault-tolerant permanent magnet motor with guaranteed postfault performance," *IEEE Trans. Ind. Electron.*, vol. 67, no. 7, pp. 5959–5970, Jul. 2020.
[28] Y. Zhang and J. Liu, "An improved Q-PLL to overcome the speed reversal problems in sensorless PMSM drive," in *Proc. IEEE 8th Int. Power Electron. Motion Control Conf.*, 2016, pp. 1884–1888.
[29] Z. Novak and M. Novak, "Adaptive PLL-based sensorless control for improved dynamics of high-speed PMSM," *IEEE Trans. Power Electron.*, vol. 37, no. 9, pp. 10154–10165, Sep. 2022.

Jun Cai (Senior Member, IEEE) received the Ph.D. degree in electrical engineering from the Nanjing University of Aeronautics and Astronautics, Nanjing, China, in 2012.

He is currently a Professor with the Nanjing University of Information Science and Technology, Nanjing, China. He is the Director of Jiangsu Engineering Research Center on Meteorological Energy Using and Control. He is also the Academic Dean with the School of Mechanical and Electrical Engineering, Anhui Jianzhu University, Hefei, China. His research interests include motor drives and wireless power transfer.

Dr. Cai is the RSA Fellow and a Senior Member CES.

Yuhan Gu received the M.S. degree in control science and engineering in 2025 from Nanjing University of Information Science and Technology, Nanjing, China, where he is current working toward the Ph.D. degree in environmental perception and intelligent control.

His research interests include motor drives and control.

Zeyuan Liu received the Ph.D. degree in electrical engineering from the Nanjing University of Aeronautics and Astronautics, Nanjing, China, in 2010.

Since 2014, he has been with the Nanjing University of Posts and Telecommunications, where he is currently an Associate Professor with the Department of Electrical Engineering. His research interests include motor drive and control.

Shoujun Song (Senior Member, IEEE) received the Dr.-Ing. degree in electrical engineering from the Technical University of Berlin, Berlin, Germany, in 2009.

He is currently a Professor with the School of Automation, Northwestern Polytechnical University. His research interests include electric machines and drives in more electric aircraft.